Electrochimica Acta 230 (2017) 316–323

Contents lists available at ScienceDirect

Electrochimica Acta

journal homepage: www.elsevier.com/locate/electacta

Prussian blue-nitrogen-doped graphene nanocomposite as hybrid electrode for energy storage applications

M. Sookhakian[a,b,c,*], W.J. Basirun[b], Mohd Asri Mat Teridi[d], M.R. Mahmoudian[a], Majid Azarang[b], Erfan Zalnezhad[c], G.H. Yoon[c], Y. Alias[a,b]

[a] University Malaya Centre for Ionic Liquids, Department of Chemistry, Faculty of Science, University of Malaya, Kuala Lumpur 50603, Malaysia
[b] Department of Chemistry, Faculty of Science, University of Malaya, Kuala Lumpur 50603, Malaysia
[c] Department of Mechanical Convergence Engineering, Hanyang University, 222 Wangsimni-ro, Seongdong-gu, Seoul, 133-791, Korea
[d] Solar Energy Research Institute, National University of Malaysia, 43600 Bangi, Selangor, Malaysia

ARTICLE INFO

Article history:
Received 11 May 2016
Received in revised form 29 January 2017
Accepted 5 February 2017
Available online 6 February 2017

Keywords:
Prussian blue
N-graphene
energy storage
cyclic voltammetry

ABSTRACT

Water-soluble Prussian blue nanoparticles (PB NPs) supported on nitrogen-doped graphene (N-graphene) with high dispersion was fabricated for high performance energy storage hybrid electrodes. An efficient loading of the PB NPs and nitrogen doping of graphene were achieved. The structure and morphology of the composite was determined by X-ray diffraction, transmission electron microscopy, Raman spectrometry and X-ray photoelectron spectrometry. The energy storage performance was assessed by cyclic voltammetry and galvanostatic charge/discharge techniques. The nanocomposite was fabricated as a hybrid battery-supercapacitor electrode and exhibited excellent performance with the highest capacity of 660 C g^{-1} at 1 A g^{-1}, which was higher than pure PB NPs and N-graphene electrodes. Moreover, the synergistic effect of N-graphene and the PB NPs prevented the N-graphene from shrinking and swelling and increased the cycle stability to 84.7% retention after 1500 cycles at 6 A g^{-1}, compared to the pure N-graphene.

1. Introduction

In recent years, supercapacitors are excellent energy storage devices due to their long-term cycling stability, high power densities and high charge/discharge rates. Supercapacitors are promising storage devices for a wide range of applications, such as hybrid electric vehicles, cordless electric tools, portable electronic equipment and backup power sources [1]. The energy stored in supercapacitors arises from individual electrostatic interactions [electrical double layer capacitor (EDLC)] and charge transfer process across the electrode-electrolyte interface (pseudocapacitance) [2], or a combination of both EDLC and pseudocapacitance in hybrid supercapacitors. The energy stored in EDLC devices is significantly lower than in pseudocapacitors due to the shrinking and swelling of the electroactive materials, which leads to a significant decrease in the cycle life during the charge/discharge process. Therefore, to overcome this problem, it is extremely necessary to combine both types of capacitive materials with high capacitance and long cycle life to develop a new generation of hybrid supercapacitors.

To date, various carbon polymorphs, such as carbon nanotubes, activated carbon, carbon onions, carbon fibers and graphene [2,3] have been widely utilized as EDLC electrodes to enhance supercapacitor performance further. Notably, graphene, a new member of the carbon family with a high surface area, rapid charge carrier mobility and excellent thermal conductivity [2], is suitable as EDLC or as the support material in pseudocapacitor electrodes. However, the aggregation of graphene during the fabrication of the supercapacitor nanostructures, could dramatically decrease the surface area [4–7], and thereby lead to a significant decrease in capacitance. Therefore, the functionalization or doping of the graphene lattice with elements such as sulfur, phosphorous boron and nitrogen is an effective step to modulate the surface chemistry and the electronic properties of graphene [8,9]. Among these heteroatoms, nitrogen is best dopant in the graphene lattice due to its similar atomic radius and valence electrons [8]. Furthermore, the graphene π-electronic system and the lone pair of the nitrogen atoms can form strong valence bonds. This will lead to a significant

* Corresponding author at: University Malaya Centre for Ionic Liquids, Department of Chemistry, Faculty of Science, University of Malaya, Kuala Lumpur 50603, Malaysia. Tel.: +603 79675330; fax: +603 79675330.
E-mail addresses: m.sokhakian@gmail.com, m.sokhakian@siswa.um.edu.my (M. Sookhakian).

http://dx.doi.org/10.1016/j.electacta.2017.02.022
0013-4686/

improvement in the electronic conductivity, charge distribution and spin density of the doped graphene, which promotes a uniform dispersion and fast nucleation growth kinetics of the nanostructures [8]. Therefore, nitrogen doping not only increases the pseudocapacitance and double-layer capacitance of graphene [10], but also enhances its ability to bind with guest molecules to improve the electrochemical performance of the nanocomposites. However, nitrogen-doped graphene (N-graphene) still shows unsatisfactory performance due to its insufficient charge capability; in addition, the shrinking and swelling of an N-graphene electrode leads to a significant reduction in the capacitance and cycle life of the supercapacitor electrode. Therefore, it has been suggested that inorganic materials such as metal oxides [10], or organic compounds such as conductive polymers [11] with fast Faradaic reaction rate, should be incorporated into the N-graphene system to improve the capacitance and cycle life of the hybrid supercapacitor electrode.

Prussian blue (PB) is an inorganic compound with a cubic framework, where the Fe(III) and Fe(II) are located on the alternating corners of a cube. The corner-shared octahedral in the Prussian blue framework is bridged by the linear $(CN)^-$ anions; the high-spin Fe(II) (S = 5/2) bonds with the N atoms, while the low-spin Fe(III) (S = 0) bonds with the C atoms [12]. Due to its high specific surface area, controllable structure, adjustable pore size and high thermal stability, PB has been widely used as an outstanding candidate in clean energy applications such as electrocatalysts, sensors and batteries, as well as electrochromic, spintronic and hydrogen storage devices [13–17]. The redox process of the Fe ions in PB could provide an electron transfer pathway. Alternatively, the crystal structure of PB promotes the reversible intercalation and extraction of ions, in organic and aqueous electrolytes [13], which is largely suitable for electrocatalytic and energy storage applications of the hybrid composite. In addition, the presence of N-graphene in the Prussian blue-N-graphene composites (PB-NGs) not only provides a platform for the formation of PB nanoparticles (NPs) to decrease the agglomeration of graphene layers, but it also promotes rapid electron transfer, which enhances the energy storage of the hybrid battery-supercapacitor electrode.

In this work, we have developed a simple process for the synthesis of a highly water-soluble PB-NG nanocomposite with excellent energy storage performance. There are no previous reports on the synthesis and energy storage performance of N-graphene in the presence of PB NPs. Although both materials are energy storage electrodes, there is a fundamental difference between a supercapacitor material such as N-graphene and PB which is a battery material, in the charge storage/release mechanism. Thus the combination of these two materials can be referred as a hybrid battery-supercapacitor electrode. The loading of PB NPs in the nanocomposites leads to the enhancement of the energy storage and cycling stability of the hybrid battery-supercapacitor electrode, compared to the pure N-graphene and pure PB NPs.

2. Experimental methods

2.1. Chemical reagents

Analytical grade chemicals were procured from Sigma Aldrich and dissolved in double-distilled water (resistance = 18.3 MΩ).

2.2. Synthesis of Prussian blue nanoparticles

In a typical procedure, 20 ml of 1.5 M $Fe(NO_3)_3$ solution were added into 40 ml of 0.5 M $K_4Fe(CN)_6$ with continuous stirring for 30 min at 70 °C to produce a dark blue PB pigment suspension. The mixture was centrifuged three times with doubly distilled water and the PB precipitate was collected and dried in air overnight. Next, 600 mg of PB pigment were dispersed in 40 ml doubly distilled water, and followed by the addition of 10 ml of a fresh solution of 50 mM $K_4Fe(CN)_6$. With vigorous stirring for 6 h, the pigment was completely dissolved, and the suspension turned a transparent blue. The purification of the PB NPs was achieved by a stirred ultrafiltration cell and membrane with a cut-off of molecular weight 3000 to remove the residual salts. This process was repeated at least five times by adding fresh doubly distilled water until the filtrate became colorless.

2.3. Synthesis of nitrogen-doped graphene

Graphite powder (1–2 μm, Aldrich) was the precursor for the graphene oxide (GO) synthesis according to the modified Hummers method [18]. The synthesis of N-graphene is described according to our previous work [19]. Briefly, 50 mL of a GO suspension in ethanol (1 mg/mL) was added with 100 mg of urea. The dispersion was heated to 80 °C with stirring until it dried. The powders were then placed in an Al_2O_3 crucible in a tube furnace and flushed with Ar gas to remove the oxygen. After the flow of Ar gas (100 sccm), the temperature was increased to 600 °C at 3 °C min^{-1} for an hour. Then, the temperature was increased to 900 °C at 5 °C min^{-1}. The temperature was held at 900 °C for 4 hours. Finally it was cooled to room temperature, to collect the as-synthesized N-graphene.

2.4. Synthesis of Prussian blue-nitrogen-doped graphene hybrids

To prepare the PB-NG hybrids, PB NPs and an N-graphene solution were mixed with a mass ratio of 2:1 with continuous stirring for 10 h to produce a dark green dispersion. The PB-NG dispersion was centrifuged three times with doubly distilled water to remove the supernatant and collect the PB-NG sediment.

2.5. Instrument characterizations

A X-ray powder diffractometer (XRD, PANalytical's Empyrean) with CuKa radiation (l = 1.54056 Å) was used to characterize the powders. A transmission electron microscope (500 kV, TEM-FEIG-4020) was utilized to examine the particle sizes and the morphology of the electrodes. The electrodes were ultrasonicated in distilled water prior to the characterization. The spectroscopic measurements were performed with an ESCALAB MK II X-ray photoelectron spectrometer (Mg excitation source) for the X-ray photoelectron spectroscopy (XPS) analysis, while a Renishaw Invia Raman Microscope instrument (laser excitation, l = 514 nm) was utilized for the Raman spectroscopy analysis. The electrochemical experiments were performed with a potentiostat/galvanostat (Autolab PGSTAT30, Ecochemie Netherlands).

2.6. Electrochemical measurements

All electrochemical measurements such as galvanostatic charge/discharge (GCD), electrochemical impedance spectroscopy (EIS), and cyclic voltammetry (CV) were conducted in a three-electrode cell system with 1 M H_2SO_4 aqueous solution as the electrolyte. A platinum wire and $Hg/Hg_2SO_4/K_2SO_4$ electrode were the counter and reference electrode, respectively. The working electrode was a glassy carbon disc with a diameter of 3 mm. The electrodes of pure PB NPs, pure N-graphene and PB-NG hybrids, were prepared by casting onto the glassy carbon surface. Typically, 5 mg of the electroactive material was dispersed in 5 ml doubly distilled water for 1 h by ultrasonication. Then, 10 μl of the suspension and 5 μl of Nafion solution (0.05% Nafion in ethyl

alcohol) were casted onto the glassy carbon surface and dried at room temperature. The mass loading for each electrode was 0.01 mg. The capacity of the hybrid electrode (C_t) was calculated from the GCD curves using the following equation:

$$C_t = \frac{I\,\Delta t}{m} \quad (1)$$

Where ΔV is the applied potential difference after a full discharge, m is the mass of the active material, Δt is the time for a full discharge and I is the discharge current. The electrochemical impedance spectra were obtained at the open circuit potential (OCP) with an amplitude of 5 mV around the OCP between 0.01 Hz to 100 kHz.

3. Results and discussions

3.1. X-ray diffraction patterns

The crystalline structures and phase compositions were investigated by XRD. Fig. 1a shows the X-ray diffractograms of graphite, GO and N-graphene. As seen in Fig. 1a for raw graphite, an intense and sharp diffraction peak (2θ) appears at 26.8°, and is attributed to the hexagonal lattice of the (002) plane with an interlayer spacing of 0.33 nm. This spacing was narrower than the GO located at 10.6° with an interlayer spacing of 0.83 nm [18]. The increase in the interlayer spacing indicates that the GO sheets were exfoliated from the bulk graphite due to the presence of carboxyl, oxygen and other functional groups. In comparison, after the GO was annealed with urea at 900 °C in Ar for 4 h, the diffractogram shows the disappearance of this strong peak along with the appearance of a broad (002) diffraction peak centered at 2θ of 24.86°, corresponding to an interlayer spacing of 0.35 nm, which indicates the formation of graphene during the annealing process from the removal of the oxygen functional groups [8]. The crystalline structures of the pure PB NPs and the PB-NG composites are illustrated in Fig. 1b. It is obvious that the PB-NG composites exhibited XRD patterns similar to those of the blank PB NPs, which indicates that the PB NPs were unaffected by the presence of N-graphene sheets; thus, N-graphene serves as a platform where the PB NPs could decorate and attach. The peaks located at the 2θ values of 17.499°, 24.780°, 30.423°, 35.261°, 39.561°, 43.521°, 50.642°, 53.941°, 57.121°, 60.162°, 63.122°, 66.002°, 68.861°, 74.341° and 77.024° can be indexed to the (200), (220), (222), (400), (420), (422), (440), (600), (620), (622), (444), (640), (642), (800) and (820) lattice planes, respectively, of cubic PB (JCPDS card no. 00-052-1907) with the lattice constants a = b = c = 10.199 Å. Notably, no typical N-graphene diffraction peaks were observed in the PB-NG composite, which could be due to the small amount of N-graphene [18].

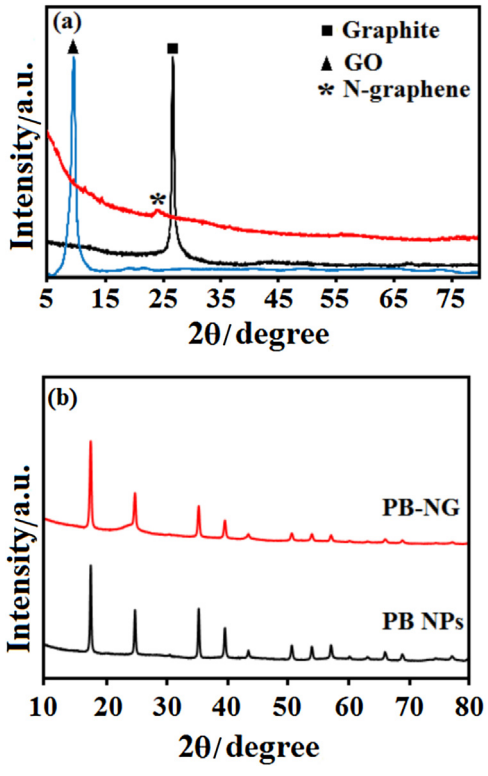

Fig. 1. (a) XRD patterns of graphite, GO and N-graphene; (b) XRD patterns of pure PB NPs and PB-NG composites.

3.2. Morphology and structure

The morphology and structure of the as-synthesized pure N-graphene nanosheets, pure PB NPs and PB-NG composites were investigated by TEM (Figs. 2 and 3). The detailed TEM image of N-graphene reveals a crumpled sheet-like layer morphology with diameters of several micrometers (Fig. 2a). The crumpling could be attributed to the defective structures formed by the exfoliation or the introduction of doped nitrogen atoms. The TEM image of pure PB NPs (Fig. 2b) clearly shows a number of particles agglomerated together due to the large surface to volume ratio of the nanoparticles, which is attributed to the absence of surfactant during the synthesis process.

A low-magnification TEM image of the PB-NG composites shows a large amount of well distributed PB NPs on the surface of the N-graphene sheets, i.e., the N-graphene sheets were fully decorated with the PB NPs (Fig. 3a). Moreover, a close-up view reveals that the individual PB NPs with cubic shape and sizes between 15–20 nm were well separated from each other; with the absence of any aggregation of the PB NPs on the N-graphene sheets (Fig. 3b).

Raman spectroscopy was also utilized to further investigate the structural and electronic properties of the as-synthesized N-graphene. Fig. 4 compares the Raman spectra of the pristine GO and N-graphene after the annealing with urea at 900 °C. The Raman spectra of GO contain three peaks located at 1359, 1588 and 2688 cm^{-1}, which corresponds to the D, G and 2D bands, respectively. The G band is the result of the in-plane bond stretch of the C-C sp^2 bond, and the D band is attributed to the different types of defects, such as the vacancy-like and sp^3 defects. These defects are the product of hydrogenation, oxidation, electron doping, domain boundaries and grain boundary edges. In addition to these three peaks, N-graphene exhibits an extra weak *D'* band located at 1710 cm^{-1} [20]. However, the major difference between N-graphene and GO is the degree of disorder, which can be observed from the intensity ratio of the D and G bands (I_D/I_G). The intensity ratio (I_D/I_G) of GO and N-graphene are 0.66 and 1.28, respectively. The increase of the (I_D/I_G) ratio implies that the annealing process created a large amount of sp^2 bonds and structural defects in the N-graphene lattice. The intensity of the 2D band is attributed to a two-phonon double-resonance phenomenon and is reciprocal to the rate of the electron-hole scattering process [20]. Therefore, the increased intensity of the 2D peak at 2703 cm^{-1} is due to the increase of the N-graphene layers after the annealing with urea [20].

To further investigate the elemental compositions and nitrogen-bonding configurations in N-graphene, XPS spectra are presented in Fig. 5. The wide-scan spectra of GO and N-graphene clearly indicate the presence of carbon and oxygen. The presence of nitrogen in the XPS spectrum of N-graphene unambiguously

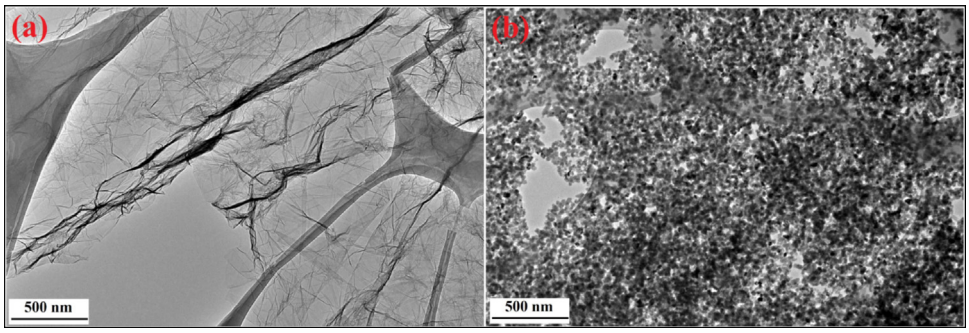

Fig. 2. TEM images of (a) pure N-graphene and (b) pure PB NPs.

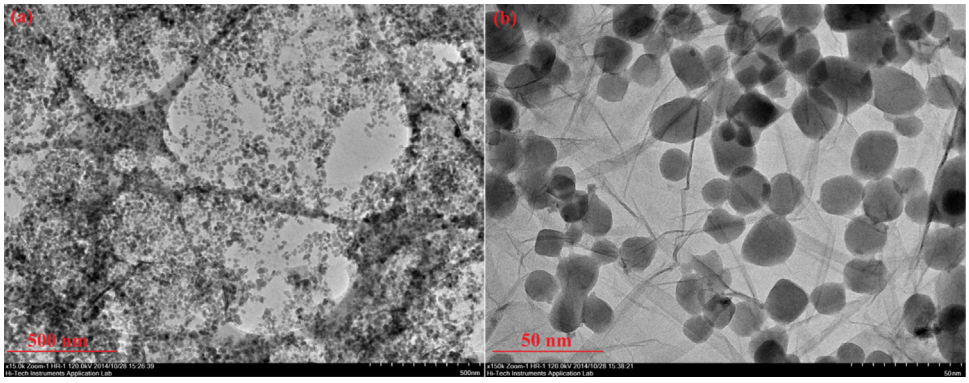

Fig. 3. (a) Low and (b) high magnification TEM images of PB-NG composite.

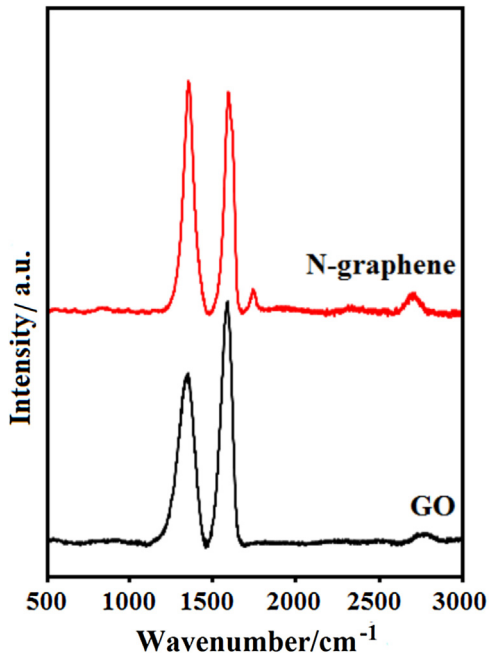

Fig. 4. Raman spectra of GO and N-graphene.

reveals that nitrogen was doped into the graphene lattice during the annealing of GO with urea (Fig. 5a). The C 1s and O 1s peaks are located at 284.5 eV (Fig. 5c) and 531.6 eV (Fig. 5a), respectively [8]. The calculated C:O atomic ratio is approximately 0.69. However, after the annealing with urea, the intensity of the O1s peak decreased significantly with the C:O atomic ratio of 2.36, which indicates a successful reduction of the GO. Moreover, the N-graphene spectrum clearly reveals the presence of the N 1s peak at 398.6 eV, with an N:C atomic ratio of 0.56 (Fig. 5a). Based on these results, urea plays two roles in the formation of N-graphene. In the first step, GO is exfoliated and reduced to graphene at 180 °C, i.e., during the pyrolysis of urea [21]. In this step, the decomposition products of urea such as cyanuric acid and melamine can polymerize into the more stable carbon nitride [22]. In the second step, the carbon nitride decomposes to release NH_3 at temperatures above 600 °C, which promotes the nitrogen doping process [23]. Furthermore, the wide-scan spectra of both the N-graphene and the PB-NG composite clearly reveal the presence of carbon, oxygen and nitrogen, while the presence of the iron peak (Fe 2p) at 708 eV in the PB-NG composites is due to the PB NPs in the nanocomposite (Fig. 5b). Notably, after the loading of the PB NPs, the intensity of the N 1s peak at 398.6 eV in the PB-NG composite increased significantly compared to the pure N-graphene. The N:C atomic ratio reached 0.86, which is another reason for the presence of the nitrogen atoms of PB NPs in the nanocomposite.

The oxygen functionalities of GO and N-graphene spectra were identified by deconvolution of the C 1s peak into three different regions. Fig. 5c is the high-resolution C 1s spectrum of the GO, deconvoluted into two strong peaks at 284.6 and 286.9 eV assigned to the C—C and C—O hydroxyl groups, respectively. The weaker peak at 288.8 eV is attributed to the O—C=O bond of GO [8]. Fig. 5d is the C 1s spectrum of N-graphene and shows the same oxygen functional groups as the GO spectrum. But the intensities of the oxygenated carbons (C—O and O—C=O) in the higher energy region (286–290 eV) show a considerable decrease after the annealing with urea, thus confirms the effective recovery of the π-electron system of graphene [8]. Moreover, the presence of the C-N groups at 285.7 eV suggests that the nitrogen atoms were doped into the graphene lattice during the annealing process with urea [24]. The deconvolution of the N 1s peak of the PB-NG composite could provide detailed information on the nitrogen

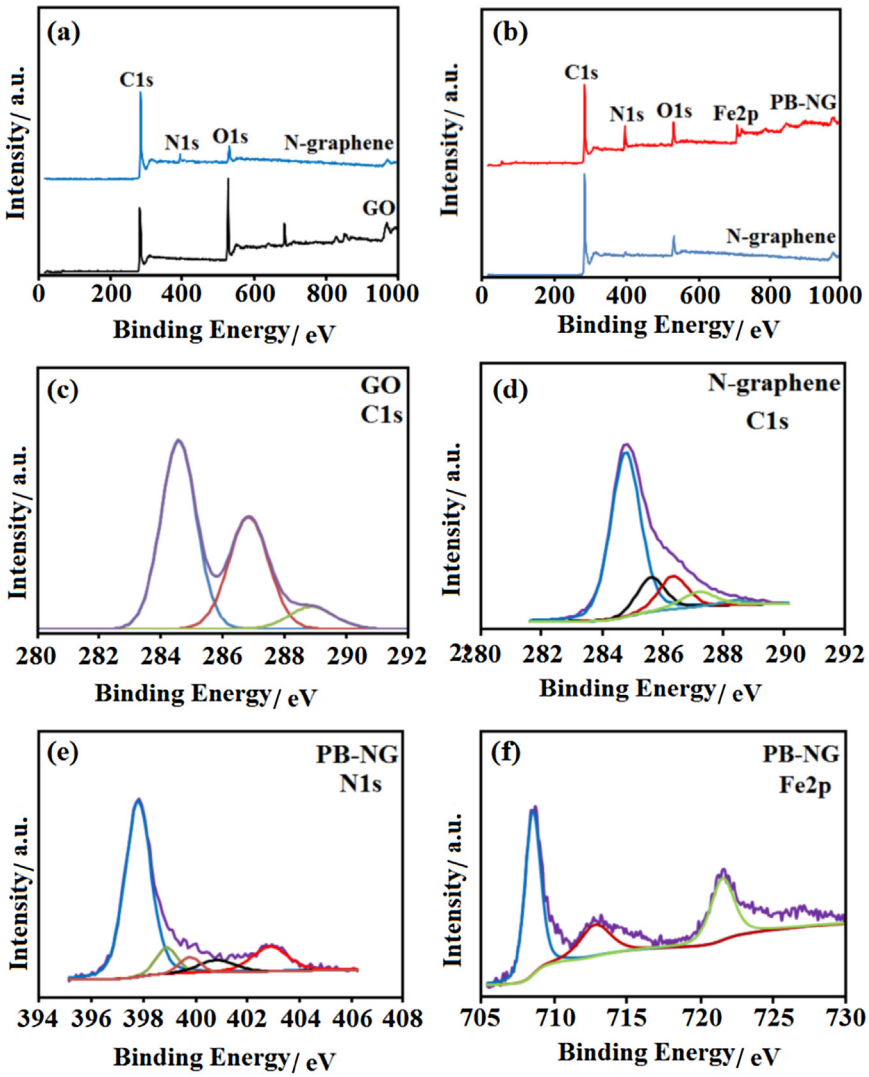

Fig. 5. (a) XPS spectra of GO and N-graphene; (b) XPS spectra of N-graphene and PB-NG composite; the high-resolution C1s spectra of (c) GO and (d) N-graphene; the high-resolution (e) N1s and (f) Fe2p spectra of the PB-NG composite.

functional groups. Fig. 5e shows that the N 1s peak could be deconvoluted into five major regions. Four peaks are related to the N-graphene (397.9, 399.8, 400.8 and 402.9 eV), and one peak is attributed to the PB NPs (398.8 eV). The nitrogen functional groups of N-graphene are assigned to four different types of N-containing groups: the pyrrolic N-C, pyridinic N-C, quaternary N-C and oxidized-N of pyridinic-N [23]. The pyridinic N-C are the N atoms located at the edges of the graphene plane and is bonded with two carbon atoms and contributes one π-electron to the π-electron system of graphene. The pyrrolic N-C is the N atoms which are bonded to two carbon atoms and donates two π-electrons to the π-electron system. The quaternary N-C are the N atoms which bonds with three carbon atoms in the graphene plane, while the pyridinic nitrogen are the oxidized nitrogen atoms, which are bonded to one oxygen atom and two carbon atoms [8,23]. Furthermore, from the deconvolution of the N 1s peak of the PB-NG nanocomposite, the peak at 398.8 eV is attributed to the C-N ($[Fe(CN)_6]^{4-}$). Fig. 5f shows the Fe XPS spectra of the PB-NG nanocomposite to elucidate the electronic states of the PB NPs. As shown in Fig. 5f, the binding energies of $Fe2p_{3/2}$ and $Fe2p_{1/2}$ are observed at 712.8 and 721.6 eV, respectively, which are attributed to the presence of Fe^{3+} [25]. The peak at 708.5 eV can be assigned to the $Fe2p_{3/2}$ of $[Fe(CN)_6]^{4-}$ [26].

3.3. Electrochemical performance

The electrochemical performance of the as-prepared PB-NG hybrid electrode was analyzed using CV, GCD and EIS measurements in 1 M H_2SO_4. Fig. 6a and b show the CV curves of the pure PB NPs and pure N-graphene at 10 mV s^{-1}. A strong pair of redox peaks is observed in the CV of the pure PB NPs, which indicates the high redox activity (Fig. 6a), and is typical for a battery electrode, not a supercapacitor one. The redox peaks are attributed to the reduction/oxidation and reversible electron transfer process of the Fe(II) and Fe(III), which is beneficial for the Faradaic process in the hybrid electrode. Compared to the pure PB NPs, the CV of the pure N-graphene electrode exhibits a rectangular shape, which is an important characteristic of a double-layer capacitor (Fig. 6b). Furthermore, a very broad peak current, observed in the CV plot of N-graphene, is attributed to the nitrogen doping in the graphene system. However, all of the CV plots of the PB-NG hybrid electrodes, at 5, 10, 30 and 50 mV s^{-1}, have a near rectangular shape, which is characteristic of double-layer capacitor. The redox peaks are the characteristics of a Faradaic process in the nanocomposite (Fig. 6c). Indeed, the oxygen groups located at the edge of the N-graphene, promotes the surface hydrophilicity in an aqueous electrolyte and improve the double layer capacitance

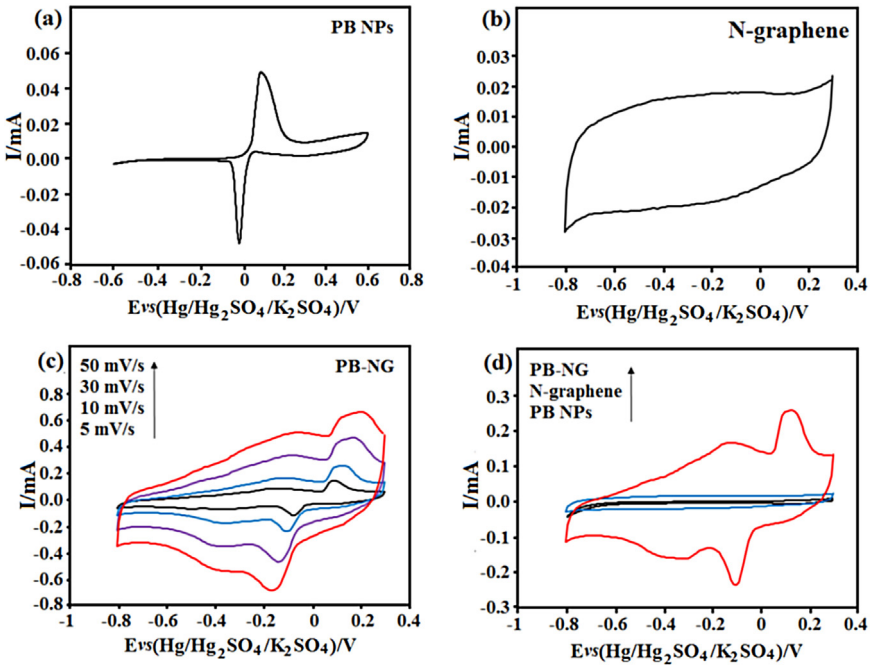

Fig. 6. (a) CV plots of (a) PB NPs and (b) N-graphene at a scan rate of 10 mV s^{-1}; (c) CV plots of PB-NG composite at scan rates of 5, 10, 30 and 50 mV s^{-1}; (d) comparative CV plots of samples at a scan rate of 10 mV s^{-1}.

properties of the composite. On the other hand, these oxygen groups interact with the Fe ions to provide the charge transfer characteristics of a pseudocapacitor, which contribute to the overall storage [27]. As seen in Fig. 6c, the anodic peak shifts to the positive direction and the cathodic peak shifts to more negative values with the increase of scan rate, which is attributed to the resistive effects of the electrode. Furthermore, the peak current increases with the increase of the scan rate, which may be attributed to a consequence of the diffusion-controlled process [28]. It is notable that the redox peaks are reproducible between 5 and 50 mV s^{-1}, which affirms the excellent rate capability of the hybrid electrode [28]. From Fig. 6a, the redox behavior of the PB suggests that the electrochemical storage mechanism is the same as a battery electrode and not due to pseudo-capacitance[29,30]. As pointed out by Brousse et al. [29] the term hybrid refers to a combination of two different types of charge storage behavior, one capacitive and the other Faradaic, in the same nanocomposite.

Fig. 6d compares the representative CV plots of the pure PB NPs, pure N-graphene and PB-NG composites at 10 mV s^{-1} in 1 M H_2SO_4. The CV of the PB-NG nanocomposite shows a significant increase in

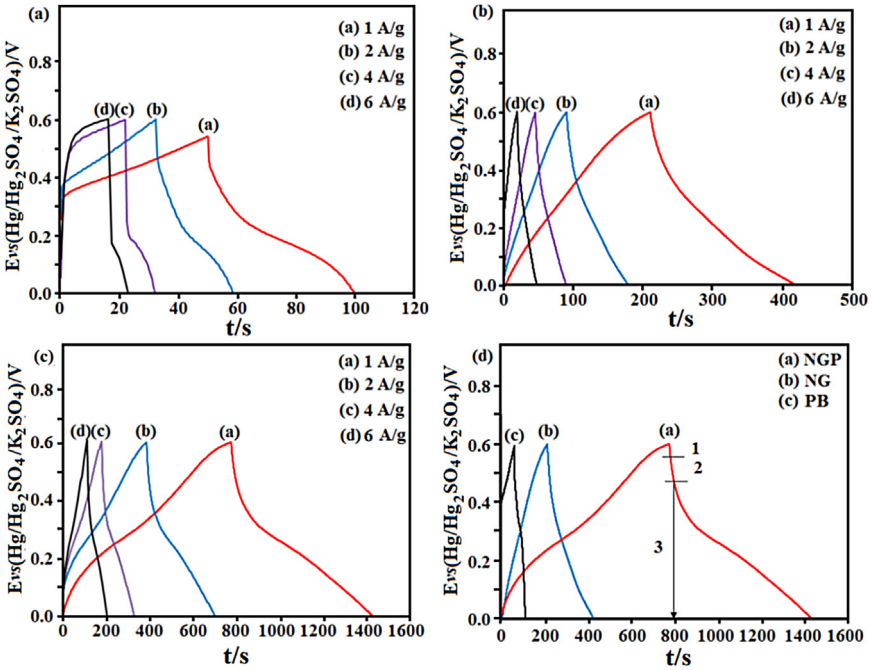

Fig. 7. GCD plots of (a) PB NPs, (b) N-graphene and (c) PB-NG composite at current densities of 1, 2, 4 and 6 A g^{-1}; (d) comparative GCD plots of samples at a current density of 1 A g^{-1}.

Table 1
Capacities obtained for the PB NPs, N-graphene and PB-NG composite at different current densities.

j/A g^{-1}	1	2	4	6
PB NPs (C g^{-1})	51	49.2	42.6	40.8
N-graphene (C g^{-1})	210	175.8	163.8	162
PB-NG (C g^{-1})	660	627.6	591.6	552

the current and total charge compared to the pure PB NPs and N-graphene electrodes at the same scan rate, which confirms that the introduction of the N-graphene significantly improves the charge storage capacity of the PB-NG hybrid nanocomposite. In contrast, the PB NPs electrode shows the lowest current and charge capacity (Fig. 6d). From the CV plots, it could be concluded that the interaction of N-graphene with a highly conductive material such as PB NPs, could introduce new pathways for the electron transfer process, hence improve the conductivity and storage properties of the hybrid electrode. Indeed, the increased surface area and porosity due to the presence of N-graphene could increase the contact area of the hybrid electrode with the electrolyte, increasing the number ions which can reach the electrode. Additionally, the increased conductivity leads to faster ion transport, thus maintaining an excellent reversibility. Therefore, the as-prepared PB-NG hybrid electrode provides high charge storage capacity for energy storage applications.

GCD measurement is a reliable technique for the analysis of the hybrid electrode performance under controlled current conditions. Fig. 7a–c show the GCD plots of hybrid electrodes between 0.0 to 0.6 V at 1, 2, 4 and 6 A g^{-1}.The calculated capacities of the hybrid electrodes at different current densities are listed in Table 1. The capacity of the pure PB NPs and pure N-graphene at 1 A g^{-1} are 51 and 210 C g^{-1}, respectively. The PB-NG hybrid gives a maximum capacity of 660 C g^{-1} at 1 A g^{-1}, which is in good agreement with the CV data. Furthermore, the capacity decreases with the increase of the charge-discharge current density. This is due to the rates of redox reaction and ion diffusion which are unable match the rapid increase in current densities [31]. However, the capacity retentions of 80%, 77% and 84%, for the pure PB NPs, pure N-graphene and PB-NG hybrids respectively, at 6 A g^{-1} signifies the excellent rate capability of the hybrid electrode, particularly at fast charge-discharge rates.

The GCD plots of the samples were compared at 1 A g^{-1} between 0 to 0.6 V *vs.* SCE (Fig. 7d). The nonlinear GCD plot of the pure PB NPs exhibits a redox behavior. In contrast, the GCD plots of the pure N-graphene exhibit an almost rectangular charge-discharge behavior, which is the characteristic of an electrochemical double layer capacitance. However, the plot of the PB-NG hybrid (Fig. 7d) consists of three regions: a sudden drop in the potential at the beginning of the discharge due to the internal resistance (IR) (region 1), a linear variation of the time and potential (region 2) due to the presence of the double layer capacitance, and the gradual deviation from linearity (region 3) due to the redox reactions at the electrode/electrolyte interface [27]. This indicates that the overall charge storage/release characteristic is a mixed contribution of a Faradaic process of a battery electrode and electrochemical double layer capacitance.

The greatly enhanced specific capacitance of the PB-NG hybrid electrode, compared to the PB NP and N-graphene electrodes, is mainly attributed to the synergistic interaction between the highly conductive and high surface area of N-graphene and the redox behavior of PB NPs. The N-graphene in the hybrid can provide a conductive pathway by forming a bridge between the adjacent PB NPs to facilitate the rapid ion transport during fast charge/discharge process. Another reason could be due to the IR loss in the three samples. Notably, Fig. 7d clearly shows that the IR loss of the PB-NG hybrid was the smallest, signifying the lowest internal resistance of the electrode. Therefore, low internal resistance leads to lower energy dissipation as heat during the charge/discharge process, which is the main reason for the capacity enhancement of the hybrid electrode.

The cycling stability of the electrodes was further evaluated using GCD for 1500 cycles at 6 A g^{-1}. The pure N-graphene showed only 71.3% capacity retention after 1500 cycles, due to the swelling and shrinking of N-graphene during the long-term cycling test. It is interesting that the pure PB NPs showed only 78.5% capacity retention, higher than the pure N-graphene. However, the PB-NG hybrid retained 84.7% of its initial capacity after 1500 cycles. The improvement in the cycling stability of N-graphene by the PB NPs is due to the synergetic effects of N-graphene and PB NPs. The PB NPs in the hybrid nanocomposite prevented the mechanical deformation due to the swelling/shrinking of the N-graphene during the long-term cycling test. Therefore, the PB-NG hybrid electrode showed an enhanced cycling stability compared to the pure PB NPs and N-graphene over a long cycling lifetime.

Electrochemical impedance spectroscopy was performed to compare the internal resistances, charge transfer kinetics and ion diffusion processes of the supercapacitor electrodes between 100 kHz and 1 mHz with an AC applied potential amplitude of 5 mV. The Nyquist plots of the hybrid electrodes are shown in Fig. 8a, with an expanded view provided in Fig. 8b. To further analyze the behavior of the hybrid electrodes, the Nyquist plots of the electrodes were fitted by a complex equivalent circuit, as shown in the inset of Fig. 8b. In the fitting circuit, R_s, R_{ct}, Q, W and C_{dl} are the solution resistance, charge transfer resistance, constant

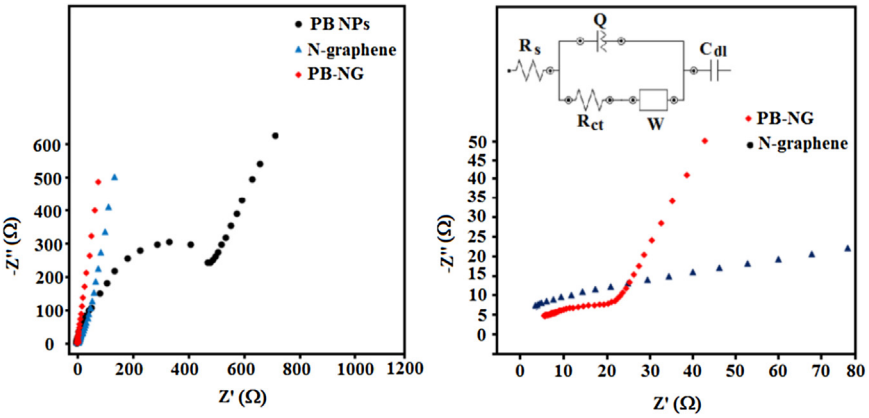

Fig. 8. (a) Nyquist plots of PB NPs, N-graphene and PB-NG composite; (b) the expanded high frequency plots; the inset is the equivalent electrical circuit to which the Nyquist plots were fitted.

phase element, Warburg coefficient and the double layer capacitance, respectively. As can be seen in Fig. 8a and b, the Nyquist plots of all electrodes are similar with each other, with a semicircle at high frequency and a linear slope at low frequency regions. The intersection point of the depressed semicircle with the real axis at high frequency region represents the R_s values. The R_{ct} values were obtained from the intersection point of the semicircle diameter at low frequency regions. The solution resistances of N-graphene and the PB-NG hybrid were almost the same (5.8 Ω), but a slightly higher solution resistance of 6.2 Ω was observed for the pure PB NPs. The PB NPs shows the highest R_{ct} value of 22 Ω, followed by N-graphene (14.8 Ω) and the PB-NG hybrid (11.3 Ω), the lowest R_{ct} value for the PB-NG hybrid is due to the higher electronic conductivity with the presence of N-graphene. Moreover, the 45° slope to the real axis in the Nyquist plots at low frequency region is known as the Warburg resistance, which is attributed to the ion diffusion toward the electrode. A larger Warburg resistance implies longer ion diffusion path lengths and slower ion movement. Among the three electrodes, the N-graphene and PB-NG hybrid exhibited more vertical lines with higher slopes than the pure PB NPs in the low frequency region. This indicates that the PB-NG hybrid showed better capacity performance due to the higher electronic conductivity and faster ion diffusion of the hybrid electrode.

4. Conclusion

Prussian blue nanoparticles of 15–20 nm in size and N-graphene sheets were synthesized and used as building blocks to prepare highly stable PB-NG hybrid battery-supercapacitor nanocomposite. The PB NPs were densely dispersed on the surface of N-graphene due to the chemical interaction between the two components. Therefore, an enhanced synergistic effect was achieved with the combination of the PB NPs redox process and the N-graphene EDLC. This led to a significant increase of the capacity of the PB-NG hybrid (660 C g^{-1}) compared to the pure PB NPs (51 C g^{-1}) and pure N-graphene (210 C g^{-1}). Moreover, the presence of PB NPs in the PB-NG hybrid led to a significant enhancement of the cycling stability of the N-graphene sheets. The presence of N-graphene in the hybrid electrode increased the electrical conductivity, which led to facile electron transport.

Acknowledgements

This research is supported by a High Impact Research MoE Grant UM.C/625/1/HIR/MoE/SC/04 from the Ministry of Education Malaysia, UMRG Program RP012A-14SUS, PG015-2013A, PG084-2013A and the University Malaya Centre for Ionic Liquids (UMCiL).

References

[1] K. Wang, X. Shi, A. Lu, X. Ma, Z. Zhang, Y. Lu, H. Wang, High nitrogen-doped carbon/Mn 3 O 4 hybrids synthesized from nitrogen-rich coordination polymer particles as supercapacitor electrodes, Dalton Trans 44 (2015) 151–157.
[2] S. Gharehkhani, S.F.S. Shirazi, S.P. Jahromi, M. Sookhakian, S. Baradaran, H. Yarmand, A.A. Oshkour, S.N. Kazi, W.J. Basirun, Spongy nitrogen-doped activated carbonaceous hybrid derived from biomass material/graphene oxide for supercapacitor electrodes, RSC Adv 5 (2015) 40505–40513.
[3] P. Yu, Y. Li, X. Zhao, L. Wu, Q. Zhang, Graphene-wrapped polyaniline nanowire arrays on nitrogen-doped carbon fabric as novel flexible hybrid electrode materials for high-performance supercapacitor, Langmuir 30 (2014) 5306–5313.
[4] M. Mahmoudian, Y. Alias, W. Basirun, P.M. Woi, M. Sookhakian, Facile preparation of MnO 2 nanotubes/reduced graphene oxide nanocomposite for electrochemical sensing of hydrogen peroxide, Sens. Actuators B- Chem 201 (2014) 526–534.
[5] S. Baradaran, E. Moghaddam, B. Nasiri-Tabrizi, W. Basirun, M. Mehrali, M. Sookhakian, M. Hamdi, Y. Alias, Characterization of nickel-doped biphasic calcium phosphate/graphene nanoplatelet composites for biomedical application, Mater. Sci. Eng. C-Mater. Biol. Appl 49 (2015) 656–668.
[6] M. Sookhakian, Y.M. Amin, R. Zakaria, S. Baradaran, M.R. Mahmoudian, M. Rezayi, M.T. Tajabadi, W.J. Basirun, Enhanced photovoltaic performance of polymer hybrid nanostructure heterojunction solar cells based on poly (3-hexylthiophene)/ZnS/ZnO/reduced graphene oxide shell-core nanorod arrays, Ind. Eng. Chem. Res 53 (2014) 14301–14309.
[7] M. Sookhakian, N. Ridwan, E. Zalnezhad, G. Yoon, M. Azarang, M. Mahmoudian, Y. Alias, Layer-by-Layer Electrodeposited Reduced Graphene Oxide-Copper Nanopolyhedra Films as Efficient Platinum-Free Counter Electrodes in High Efficiency Dye-Sensitized Solar Cells, J. Electrochem. Soc 163 (2016) D154–D159.
[8] M. Tajabadi, W. Basirun, F. Lorestani, R. Zakaria, S. Baradaran, Y. Amin, M. Mahmoudian, M. Rezayi, M. Sookhakian, Nitrogen-doped graphene-silver nanodendrites for the non-enzymatic detection of hydrogen peroxide, Electrochim. Acta 151 (2015) 126–133.
[9] M. Tajabadi, M. Sookhakian, E. Zalnezhad, G. Yoon, A. Hamouda, M. Azarang, W. Basirun, Y. Alias, Electrodeposition of flower-like platinum on electrophoretically grown nitrogen-doped graphene as a highly sensitive electrochemical non-enzymatic biosensor for hydrogen peroxide detection, Appl. Surf. Sci 386 (2016) 418–426.
[10] Z. Ma, X. Huang, S. Dou, J. Wu, S. Wang, One-Pot Synthesis of Fe2O3 Nanoparticles on Nitrogen-Doped Graphene as Advanced Supercapacitor Electrode Materials, J. Phys. Chem. C 118 (2014) 17231–17239.
[11] S. Herrmann, C. Ritchie, C. Streb, Polyoxometalate-conductive polymer composites for energy conversion, energy storage and nanostructured sensors, Dalton Trans 44 (2015) 7092–7104.
[12] Y. Lu, L. Wang, J. Cheng, J.B. Goodenough, Prussian blue: a new framework of electrode materials for sodium batteries, Chem. Commun 48 (2012) 6544–6546.
[13] P. Nie, L. Shen, H. Luo, B. Ding, G. Xu, J. Wang, X. Zhang, Prussian blue analogues: a new class of anode materials for lithium ion batteries, J. Mater. Chem. A 2 (2014) 5852–5857.
[14] E. Nossol, A.J.G. Zarbin, Transparent films from carbon nanotubes/Prussian blue nanocomposites: preparation, characterization, and application as electrochemical sensors, J. Mater. Chem 22 (2012) 1824–1833.
[15] V.D. Neff, Electrochemical oxidation and reduction of thin films of Prussian Blue, J. Electrochem. Soc 125 (1978) 886–887.
[16] V.D. Neff, Some performance characteristics of a Prussian blue battery, J. Electrochem. Soc. (United States) 132 (1985).
[17] P.J. Kulesza, K. Miecznikowski, M.A. Malik, M. Galkowski, M. Chojak, K. Caban, A. Wieckowski, Electrochemical preparation and characterization of hybrid films composed of Prussian blue type metal hexacyanoferrate and conducting polymer, Electrochim. Acta 46 (2001) 4065–4073.
[18] M. Sookhakian, Y. Amin, R. Zakaria, W. Basirun, M. Mahmoudian, B. Nasiri-Tabrizi, S. Baradaran, M. Azarang, Significantly improved photocurrent response of ZnS-reduced graphene oxide composites, J. Alloy. Compd 632 (2015) 201–207.
[19] M.A. Teridi, W. JefferyáBasirun, W.J. Silva, F. KurtáShneider, S. JooáLee, H. PiláKim, A.R. bináMohd Yusoff, Plasmon enhanced organic devices utilizing highly ordered nanoimprint gold nanodisks and nitrogen doped graphene, Nanoscale (2015).
[20] Z. Zafar, Z.H. Ni, X. Wu, Z.X. Shi, H.Y. Nan, J. Bai, L.T. Sun, Evolution of Raman spectra in nitrogen doped graphene, Carbon 61 (2013) 57–62.
[21] S. Podsiadło, Stages of the synthesis of indium nitride with the use of urea, Thermochim. Acta 256 (1995) 375–380.
[22] Y. Sakata, K. Yoshimoto, K. Kawaguchi, H. Imamura, S. Higashimoto, Preparation of a semiconductive compound obtained by the pyrolysis of urea under N 2 and the photocatalytic property under visible light irradiation, Catal. Today 161 (2011) 41–45.
[23] J. Jin, X. Fu, Q. Liu, Y. Liu, Z. Wei, K. Niu, J. Zhang, Identifying the active site in nitrogen-doped graphene for the VO2+/VO2+ redox reaction, ACS Nano 7 (2013) 4764–4773.
[24] L. Li, Y. Dou, L. Wang, M. Luo, J. Liang, One-step synthesis of high-quality N-doped graphene/Fe 3 O 4 hybrid nanocomposite and its improved supercapacitor performances, RSC Adv. 4 (2014) 25658–25665.
[25] L. Zhang, A. Zhang, D. Du, Y. Lin, Biosensor based on Prussian blue nanocubes/reduced graphene oxide nanocomposite for detection of organophosphorus pesticides, Nanoscale 4 (2012) 4674–4679.
[26] L. Cao, Y. Liu, B. Zhang, L. Lu, In situ controllable growth of prussian blue nanocubes on reduced graphene oxide: facile synthesis and their application as enhanced nanoelectrocatalyst for H2O2 reduction, ACS Appl. Mater. Interfaces 2 (2010) 2339–2346.
[27] A.N. Grace, R. Ramachandran, M. Vinoba, S.Y. Choi, D.H. Chu, Y. Yoon, S.C. Nam, S.K. Jeong, Facile Synthesis and Electrochemical Properties of Co3S4-Nitrogen-Doped Graphene Nanocomposites for Supercapacitor Applications, Electroanalysis 26 (2014) 199–208.
[28] D. Ghosh, S. Giri, M. Moniruzzaman, T. Basu, M. Mandal, C.K. Das, α MnMoO 4/graphene hybrid composite: high energy density supercapacitor electrode material, Dalton Trans 43 (2014) 11067–11076.
[29] T. Brousse, D. Bélanger, J.W. Long, To be or not to be pseudocapacitive? J. Electrochem. Soc 162 (2015) A5185–A5189.
[30] P. Simon, Y. Gogotsi, B. Dunn, Where do batteries end and supercapacitors begin? Science 343 (2014) 1210–1211.
[31] Y. Liu, Y. Ma, S. Guang, H. Xu, X. Su, Facile fabrication of three-dimensional highly ordered structural polyaniline–graphene bulk hybrid materials for high performance supercapacitor electrodes, J. Mater. Chem. A 2 (2014) 813–823.